Materials Science in Semiconductor Processing 82 (2018) 54–61

Contents lists available at ScienceDirect

Materials Science in Semiconductor Processing

journal homepage: www.elsevier.com/locate/mssp

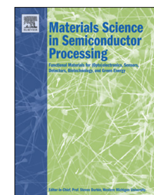

Characterization of recrystallized depth and dopant distribution in laser recovery of grinding damage in single-crystal silicon

Keiichiro Niitsu[a], Yu Tayama[b], Taketoshi Kato[b], Hidenobu Maehara[b], Jiwang Yan[c,*]

[a] School of Integrated Design Engineering, Graduate School of Science and Technology, Keio University, Hiyoshi 3-14-1, Kohoku-ku, Yokohama 223-8522, Japan
[b] SpeedFam Co., LTD., Ohgami 4-2-37, Ayase 252-1104, Kanagawa, Japan
[c] Department of Mechanical Engineering, Faculty of Science and Technology, Keio University, Hiyoshi 3-14-1, Kohoku-ku, Yokohama 223-8522, Japan

ARTICLE INFO

Keywords:
Single-crystal silicon
Subsurface damage
Laser recovery
Recrystallization depth
Raman spectroscopy
Dopant concentration

ABSTRACT

A nanosecond pulsed Nd:YAG laser was irradiated on a boron-doped single-crystal silicon wafer with a diamond grinding finish to recover the grinding-induced subsurface damage. In order to visualize and measure the depth of the laser melted/recrystallized layer, small-angle beveled polishing was performed in pure water followed by KOH etching. It enabled the direct observation of the recrystallized region using a differential interference microscope and the measurement of its depth using a white light interferometer. Crystallinity analysis of the recrystallized region was carried out by using laser micro-Raman spectroscopy, and the dopant concentration profile was characterized by using radio frequency glow discharge optical emission spectrometry (rf-GD-OES). The results showed that the crystallinity and boron distribution in the recrystallized region changed after laser recovery. The dopant concentration becomes higher at the boundary of the recrystallized region and the bulk. This study demonstrates the possibility of boron concentration control by using suitable laser parameters.

1. Introduction

Silicon is widely used in semiconductor industry. Currently, silicon wafers with a diameter of 300 mm are used mainly for the production of various electronics products. Usually, silicon substrates are produced by slicing, lapping, grinding and chemo-mechanical polishing (CMP) processes. Such mechanical machining processes cause subsurface damages, such as amorphous layers, dislocations, and microcracks, in silicon wafers [1–3]. Conventional grinding causes the formation of subsurface damage up to a depth of 2 – 5 µm [4]. By using electrical in-process dressing (ELID) grinding with extremely fine abrasive grains, the depth of damaged layer can be reduced to 0.4 – 1.3 µm [5]. However, it is extremely difficult to completely eliminate the subsurface damage layer through mechanical approaches which require physical contact.

As an alternative, Yan et al. successfully recovered subsurface damage generated by diamond machining in single-crystal silicon wafers, using laser recovery [6–8]. Laser recovery technology must be distinguished from laser annealing. Laser annealing can be used to rearrange impurities from strongly disordered material which is induced by ion beam, and produce poly-crystalline material from amorphous material. On the other hand, laser recovery technology can be used to selectively melt and recrystallize the machining-damaged subsurface layers including amorphous layers, dislocations, and microcracks, and reproduce a single-crystalline structure identical to that of the bulk. Furthermore, laser recovery technology can produce a low surface roughness in comparison to conventional grinding. Thus, laser recovery technology is expected to be more suitable as post-grinding process than the current chemical polishing. However, in order to apply the laser recovery technology to the processing of silicon wafers with various depths of subsurface damage, it is important to investigate and establish the laser recoverable depth, i.e., the depth of laser-induced silicon melting and recrystallization.

The depth of laser-affected layers in amorphous silicon can be measured by cross-sectional observation of the sample, as done in laser annealing. Since laser irradiation changes the surface structure from amorphous to poly-crystalline state, a clear boundary can be distinguished between the recrystallized layer and the amorphous bulk [9–11]. In laser recovery, however, it is difficult to directly observe the recovered layer in single-crystal silicon because there is no identifiable boundary between the recovered layer and the bulk when observation is performed with a scanning electron microscope (SEM) or a transmission electron microscope (TEM). Simulation has also been used to estimate the laser-induced recrystallized depth [6,12–14], but to date, there has been no experimental method to validate the simulated results.

* Corresponding author.
E-mail address: yan@mech.keio.ac.jp (J. Yan).

https://doi.org/10.1016/j.mssp.2018.03.029
Received 1 December 2017; Received in revised form 4 February 2018; Accepted 22 March 2018
1369-8001/ © 2018 Elsevier Ltd. All rights reserved.

Downloaded from Yan Laboratory, Keio University at http://www.yan.mech.keio.ac.jp. Redistribution is subject to copyright licence from the journal publisher.

In order to make this recovery boundary visible, the use of small-angle beveled polishing and etching is proposed. By polishing at a small-angle to the top surface, the recrystallized region can be extended in the depth direction. Therefore, the small-angle beveled polishing process reveals greater details of the recrystallized depth profile and its crystallinity than a standard cross-sectional polishing process (polished at 90° to the top surface). It is known that in laser irradiation, the melting and recrystallizing process cause dopant movement in the irradiated region, and the dopant concentration becomes maximum at the maximum melt depth [15–19]. This dopant distribution gives rise to a different etching rate between the high dope concentration region and low concentration region [20]. Thus, through etching, a boundary of the recrystallized region is thought to appear on the beveled polished surface. From this boundary, it may be possible to measure the recrystallized depth.

The purpose of this study is to characterize the recrystallized depth and dopant distribution in laser recovery of grinding damage in single-crystal silicon. This will be realized by using a new visualization method based on small-angle beveled polishing and subsequent chemical etching. The success of the proposed method will contribute greatly to the visualization and clarification of the laser recovery mechanism and the optimization of other laser melting processes of single-crystal silicon.

2. Methods

The laser recovery mechanism of a ground silicon surface is shown in Fig. 1. Generally, grinding will induce subsurface damages in silicon, such as amorphous layers, dislocations, and microcracks (Fig. 1a). After a laser pulse is irradiated on the surface, a top-down melted layer will be generated and it becomes thicker and thicker when laser irradiation continues, reaching the defect-free bulk region (Fig. 1b-c). After laser irradiation, bottom-up epitaxial growth begins from the defect-free bulk which acts as a seed crystal (Fig. 1d-e) [6–8]. In this way, a defect-free single-crystalline structure is obtained in the laser-irradiated region (Fig. 1f).

To visualize the laser melted/recrystallized layer of a ground silicon sample, small-angle beveled polishing is proposed. A frosted silica glass pad was used as the polisher, without using abrasive grains. The beveled angle is set to less than 1° in order to enlarge the observation area of the laser-recrystallized region which is extremely thin, down to the submicron level. A schematic diagram of visualization mechanism of the recrystallized region is shown in Fig. 2. The recrystallized region boundary on beveled polished surface is not visible before etching (Fig. 2a). After etching with a KOH solution, the recrystallized region on the beveled polished surface becomes visible due to an elevated boundary between the bulk and the recrystallized region (Fig. 2b). Fig. 2c-e present the cross-section taken along the black dotted line in Fig. 2a-b, and these figures indicate the mechanism of elevated boundary generation. The top surface is flattened by polishing, and the laser-recrystallized region has a boron concentration gradient. The center of the laser-irradiated region has lower dopant concentration than the outer region. During KOH etching (Fig. 2d), the etching rate of the high concentration region is lower than that of the low concentration region [20]. As a consequence, an elevated boundary is generated on the polished surface as shown in Fig. 2e, which is identifiable by microscopic observation.

3. Experimental procedures

Boron-doped P^{++} single-crystal silicon (1 0 0) wafers machined by precision grinding using diamond abrasive grains (Average grain size

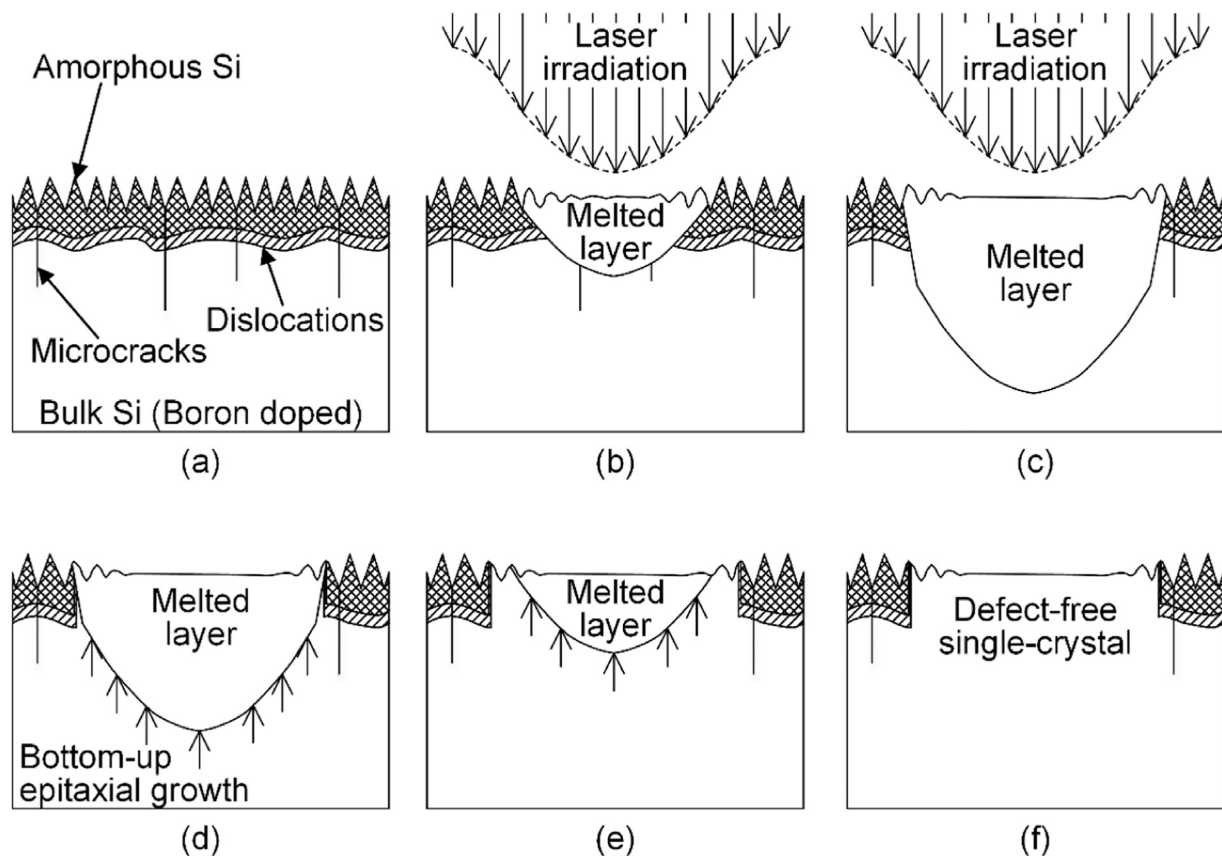

Fig. 1. Schematic diagram of laser recovery mechanism for a ground silicon surface: (a) silicon wafer with subsurface damage, (b) start of laser irradiation, (c) formation of top-down melted layer, (d) after laser irradiation, (e) bottom-up epitaxial growth from the defect-free bulk, and (f) a defect-free single-crystalline structure in the laser-irradiated region.

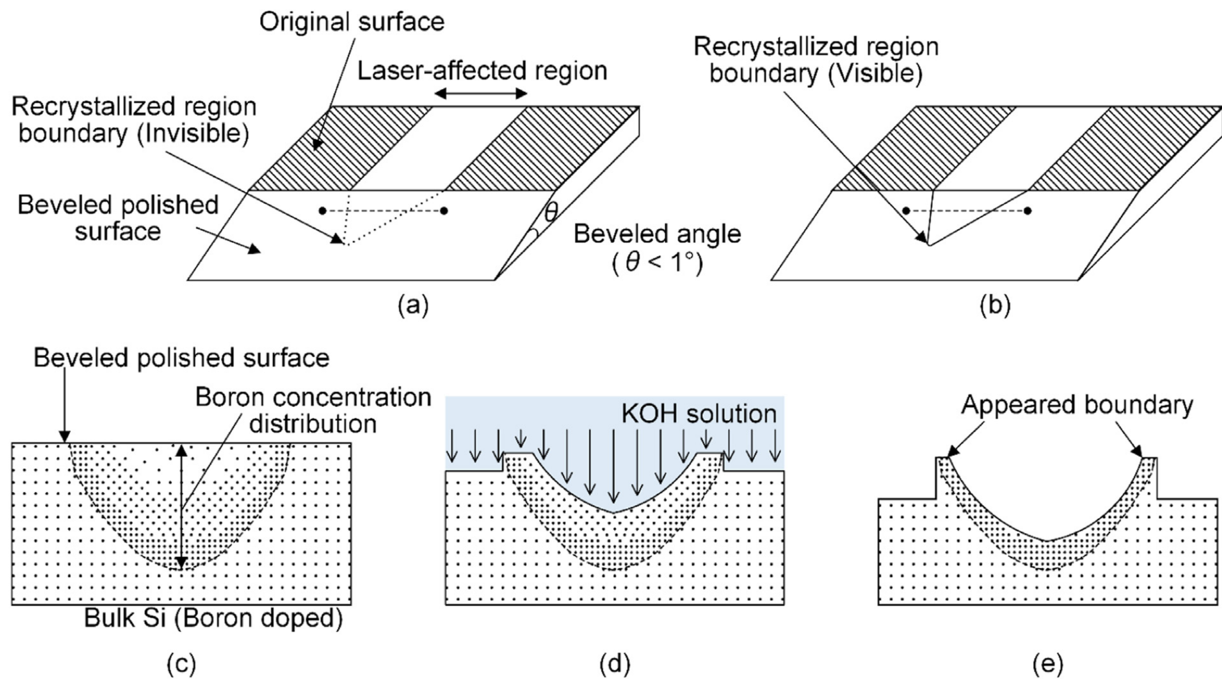

Fig. 2. Schematic diagram of visualizing recrystallized region mechanism by KOH etching. 3D topography of beveled polished silicon wafer (a) before etching, and (b) after etching. The cross-section taken along the black dotted line in (a-b): (a) boron concentration gradient in the recrystallized layer, (d) KOH etching according to different etching rates, and (e) an elevated boundary on the polished surface after etching.

Table 1
Laser irradiation conditions.

Laser type	Nd:YAG laser	
Wavelength (nm)	532	
Environment	In air	
Beam profile	Gaussian	
Beam diameter (µm)	85	
Number of pulses per unit area	100	
Pulse width (ns)	15.6	48.4
Repetition frequency (kHz)	1	10
Average power (mW)	70, 90, 110	700, 900, 1100
Laser fluence (J/cm^2)	1.23, 1.59, 1.94	
Laser peak power (kW)	4.49, 5.77, 7.05	1.45, 1.86, 2.27
Scanning speed (mm/s)	0.85	8.5

8.5 ± 0.7 µm) were used as workpiece. The resistibility of the wafers was 0.004 – 0.007 Ω·cm. The silicon wafers were cut into 10 mm × 8 mm chips. The sample was irradiated by a Nd:YAG laser system, LR-SHG, produced by MEGAOPTO Co., Ltd. The excitation light source was a laser diode, and the laser system was completely air cooled. The wave length was 532 nm. By computer control of the laser system and a galvanometer mirror, laser irradiation could be performed over the entire silicon wafer surface. The laser beam diameter was 85 µm and the beam had a Gaussian energy distribution. Pulse widths of 15.6 and 48.4 ns were used at a repetition frequency of 1 and 10 kHz, respectively. Various average laser powers were used, corresponding to laser fluence in the range of 1.23 – 2.11 J/cm^2. To keep the number of irradiation per unit area constant, the laser scanning speed was set to 0.85 and 8.5 mm/s, according to repetition frequency 1 and 10 kHz. The laser irradiation conditions are summarized in Table 1.

After laser irradiation, small-angle beveled polishing was performed. As shown in Fig. 3, a frosted silica glass pad was used for polishing. The frosted silica glass was produced by silicon carbide abrasive lapping. Pure water was used as polishing fluid. An abrasion-resistant ceramic plate was used to adjust the beveled angle precisely ($\theta < 1°$). The small-angle can be precisely maintained by using the high-stiffness frosted silica glass, which cannot be maintained by other kinds of polishing pads.

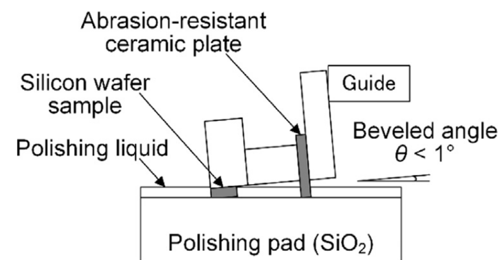

Fig. 3. Schematic diagram of small-angle beveled polishing by using a frosted silica glass polishing pad with pure water.

In order to visualize the laser-recrystallized layer on the beveled polished surface, KOH solution etching was performed. The etching time was set to 10 – 13 min. In addition, the concentration of the KOH solution was 0.5 mol/L (0.56%) and the temperature of the solution was 21 °C. A low concentration of solution was used at a low temperature to enable a low etching rate down to a few nm/min. The etching time was determined on the basis of pre-experiments. We found that if the etching time was too short, there was no clearly boundary between the irradiated and the unirradiated regions on the beveled polished surface. If the etching time was too long, however, it became difficult to distinguish the boundary due to the sample was over etched.

To examine surface topography, the sample surface was observed using a differential interference contrast microscope (Optiphot200, NIKON INSTECH Co., Ltd., Japan) and a white-light interferometer (Talysurf CCI 1000, AMETEK Taylor Hobson Ltd., UK). The vertical resolution of the white-light interferometer was 0.01 nm, while the lateral resolution was 350 nm. A laser micro-Raman spectrometer (NRS-3100, JASCO Co., Japan) was used to examine the surface crystal structure. The laser wavelength of the spectrometer was 532 nm. The dopant concentration profile of the silicon wafers was characterized by using a radio frequency glow discharge optical emission spectrometer (rf-GD-OES, GD-Profiler 2™, Horiba Jobin Yvon, France). For the elemental analysis by rf-GD-OES, two plane irradiated silicon wafer

Table 2
Laser irradiation conditions for preparing sample for elemental analysis.

Repetition frequency (kHz)	10
Pulse width (ns)	48.4
Average power (mW)	800, 900
Laser fluence (J/cm^2)	1.41, 1.59
Laser peak power (kW)	1.65, 1.86
Scanning speed (mm/s)	8.5
Scan interval (μm)	22.8, 11.4

samples were used. The laser irradiation conditions for these two samples are shown in Table 2

4. Results and discussion

4.1. Surface topography analysis

Fig. 4a shows the differential interference contrast morphology of the irradiated silicon wafer surface after beveled polishing and KOH etching. Laser-irradiated conditions were: laser peak power 2.27 kW, scanning speed 8.5 mm/s, and pulse width 48.4 ns. The beveled angle was 0.79°, which was confirmed by measuring the surface profile after polishing. The recrystallized region could be identified on the beveled polished surface, as shown in Fig. 4a. In addition, there were striped arc patterns in the recrystallized region on the surface. Fig. 4b shows the three-dimensional surface topography of beveled polished surface. In the Fig. 4b, the original surface was hidden due to the height limitation. There was a V-shaped boundary between the irradiated and the unirradiated regions on the polished surface. In addition, the irradiated region near the top surface was slightly sunk. Fig. 4c shows the cross-sectional profile taken along the dotted line in Fig. 4b. The height of the boundary was approximately 20 nm, and the depth of the sunken region was around 10 nm. The surface features on the polished surface such as the boundary, the striped arc patterns and the sunken region, may be caused by the different etching rate within the irradiated region. The etching rate of the boundary region, which was recrystallized earlier with higher dopant concentration, was lower than that of the center region, which was recrystallized lately with lower dopant concentration.

Combined plots of cross-sectional profiles of top surfaces and recrystallized regions under various laser irradiation conditions are shown in Fig. 5. It can be seen that the shapes of most laser-affected regions roughly follow the Gauss distribution indicated by the gray lines, which were calculated by the following equation:

$$f(r) = A\exp\left(-2\frac{r^2}{b^2}\right) \quad (1)$$

where r is the distance from the laser beam center, A is the maximum melt depth, and b is radius of beam spot (42.5 μm in this study). It is known from one-dimensional simulation of laser-induced crystallization of amorphous silicon thin films that the maximum melt depth increases almost linearly with laser energy density [12]. In case of laser irradiation where the laser beam has a Gaussian distribution of energy density, the distribution of temperature rise follows the Gauss

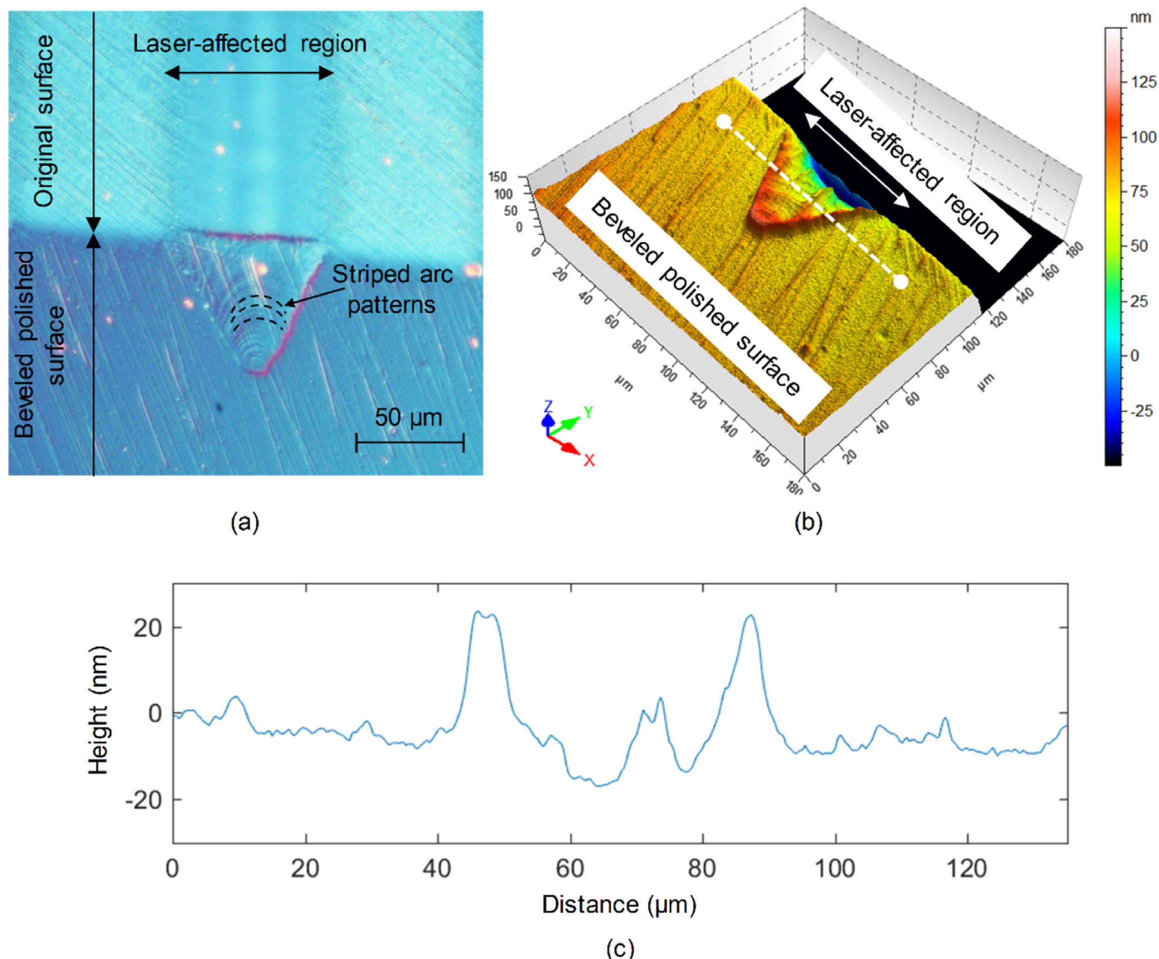

Fig. 4. (a) Differential interference contrast morphology of the irradiated silicon wafer surface after beveled polishing and KOH etching, (b) three-dimensional surface topography, (c) cross-sectional profile of the dotted line in (b).

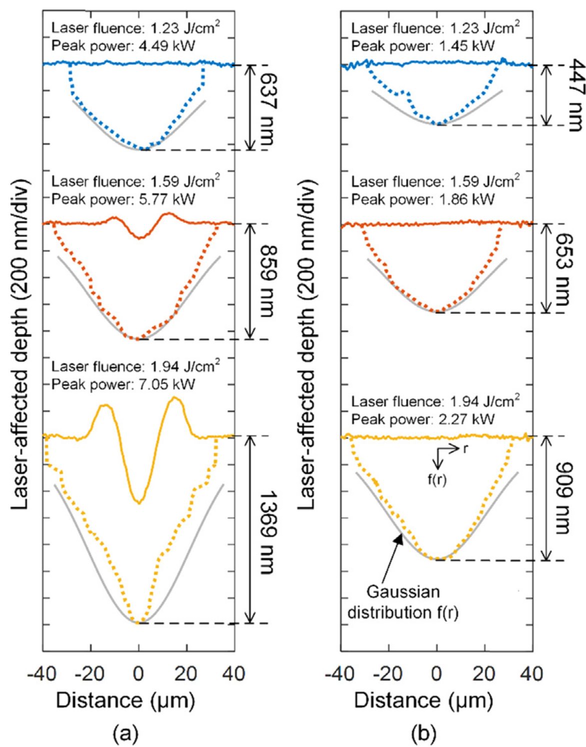

Fig. 5. Combined plots of cross-sectional profiles of top surfaces and recrystallized regions under the following conditions: (a) pulse frequency 1 kHz and pulse width 15.6 ns, and (b) pulse frequency 10 kHz and pulse width 48.4 ns.

distribution. Accordingly, the shapes of the laser-affected regions in this study roughly followed the Gauss distribution. Fig. 5 also shows that the recrystallized depth increased with laser power. Even if the laser fluence was the same, the recrystallized region under a pulse width of 15.6 ns was deeper than that of 48.4 ns due to the different laser peak power. Furthermore, in case of 15.6 ns pulse width, surface grooves were generated at laser peak powers above 5.77 kW. The shape of the recrystallized region became different from the Gaussian distribution at a peak power of 7.05 kW. This may be due to influence of the surface grooves and pile-ups, which changes laser absorption. In contrast, when using a longer pulse (~48.4 ns), the surface remained flat without grooves and pile-ups.

4.2. Evaluation of crystallinity

Fig. 6 shows the Raman spectra of original surface, beveled surface, laser-irradiated top surface, and laser-irradiated beveled surface after etching, respectively. For comparison, the spectrum of a reference CMP wafer is also shown. Laser irradiation conditions were: laser peak power 2.27 kW, scanning speed 8.5 mm/s, and pulse width 48.4 ns. The single-crystal silicon peak (521 cm^{-1} [21]) was observed each spectrum. The peak height of the original surface spectrum at 521 cm^{-1} was lower than that of the other spectra. In contrast, the peak height of original surface spectrum at 470 cm^{-1} was higher than that of the other spectra. The broad peak at 470 cm^{-1} shows amorphous silicon [21]. These results indicate two points; firstly, it indicates that laser irradiation generated single-crystal silicon from amorphous silicon, and secondly that beveled polishing by the frosted silica glass did not produce an amorphous layer. The spectra of the beveled surface and laser-irradiated top surface were very similar to the spectrum of the CMP wafer. On the other hand, it is noted that the peak height of laser-irradiated beveled surface spectrum at 521 cm^{-1} was lower than those for the reference CMP wafer, the beveled surface, and laser-irradiated top surface. In order to analyze in greater detail, mapping measurement was carried out.

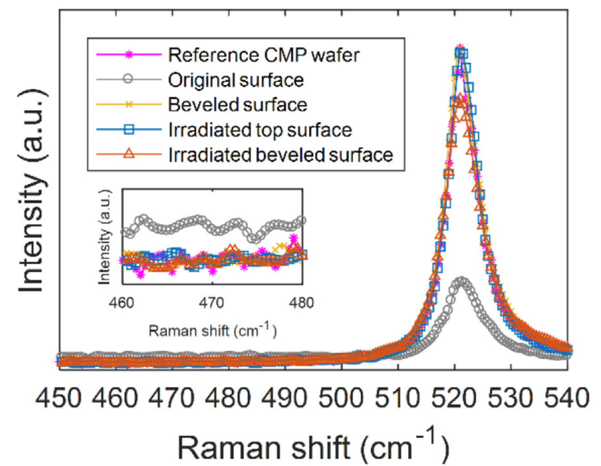

Fig. 6. Raman spectra of original surface, beveled surface, laser-irradiated top surface, and laser-irradiated beveled surface after etching. For comparison, the spectrum of a reference CMP wafer is also shown.

Fig. 7a shows the surface micrograph of a laser-irradiated surface after beveled polishing and etching. The region surrounded by the red line was characterized by Raman spectroscopy mapping. Fig. 7b shows the Raman mapping result at the single-crystal silicon peak (521 cm^{-1}). The peak height at the original surface region without laser irradiation was significantly lower than the irradiated region. This is due to the formation of an amorphous layer on the ground surface. In contrast, the peak height at the laser-irradiated region, including the beveled polished region, was high. According to the results of Fig. 6 and Fig. 7b, where no amorphous peak was observed on the beveled polished surface, it can be said that beveled polishing did not cause amorphization of silicon. In Fig. 7b, it is noted that the peak height at the lower part of the recrystallized region was slightly lower than that of the bulk region. Fig. 7c shows Raman mapping of the full width of half maximum (FWHM) at the 521 cm^{-1} peak, which is an indicator of crystallinity. The FWHM of the recrystallized region on polished surface was higher than that of the irradiated top surface. This indicates the crystallinity of the lower region near the boundary with the bulk is lower than the upper region. Fig. 7d shows Raman mapping of peak shift from 521 cm^{-1}, which is an indicator of residual stress. There was no significant peak shift observed from Fig. 7d. From these mapping results, it can be concluded that the change in crystallinity is caused by boron concentration, rather than residual stress. Furthermore, decreasing peak height of laser-irradiated beveled surface at 521 cm^{-1} is thought to be due to peak broadening. This broadening is caused by changing crystallinity.

4.3. Elemental analysis

Fig. 8 shows the change of boron concentration in silicon with depth from surface under various laser peak power at a pulse width of 48.4 ns. The concentration of boron was very low at the top surface and gradually increased with melt depth. A pile-up of boron at the maximum melt depth (642 nm) was observed under a laser peak power of 1.86 kW. This result agrees well with the recrystallized depth profile of Fig. 5b. Also, this concentration gradient is in agreement with the result of FWHM Raman mapping (Fig. 7c). These results confirm that the crystallinity change was caused by laser-induced boron concentration change.

According to the results of the Raman mapping and the boron concentration profile in silicon, there were heterogeneous boron concentration distribution in laser-recrystallized layer. The etching rate of the high concentration region is lower than that of the low

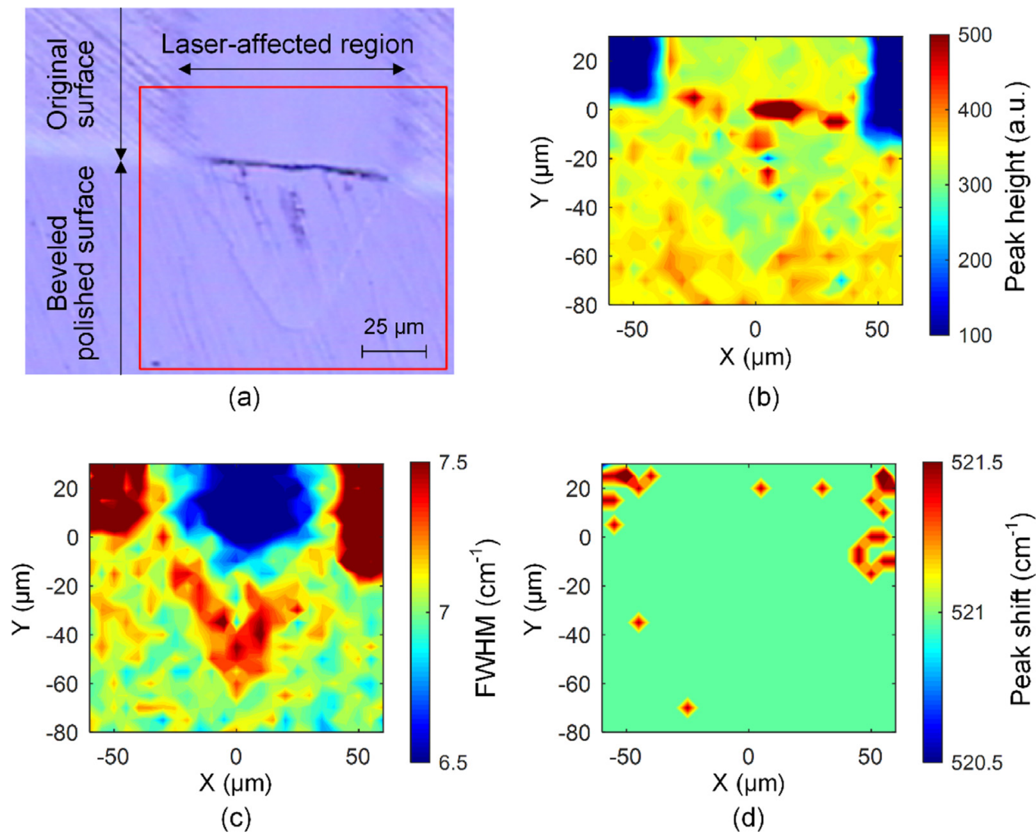

Fig. 7. (a) Surface micrograph, and Raman mapping image of (b) peak hight, (c) FWHM, and (d) peak shift, at 521 cm^{-1}.

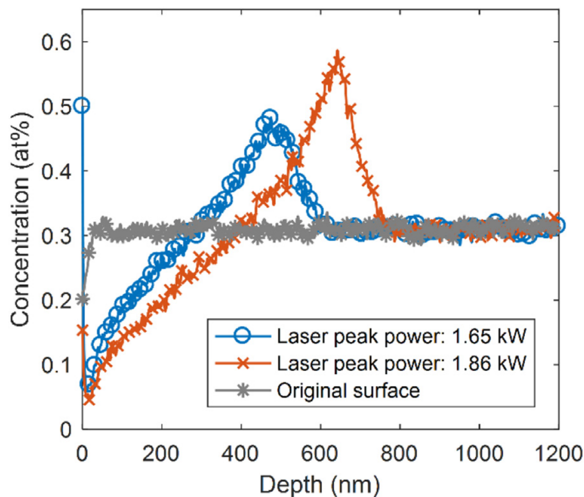

Fig. 8. Change of boron concentration in silicon with respect to depth from surface.

concentration region [20]. In other word, the etching rate of boundary recrystallized and bulk region is lower than that of bulk region. Therefore, this boron concentration distribution in laser-recrystallized layer caused different etching rate on beveled polished surface. As these results, by using KOH etching, the V-shaped boundary in Fig. 4b was produced between the irradiated and the unirradiated regions on the beveled polished surface.

In addition, in Fig. 8, the boron concentration profile changes with laser peak power. As these results, boron concentration is controllable in laser recovery by using suitable laser parameters.

4.4. Discussion on laser-induced dopant movement

Experiment and simulation results from previous studies have shown that in liquid silicon, there is coexistence of two different bonding species, namely, metallic and covalent bonding [22–27]. Fig. 9 shows the schematic diagram of the two types of liquid silicon structures with boron atoms. The metallic bonding composes high-density liquid (HDL) (Fig. 9a) while the covalent bonding makes low-density liquid (LDL) (Fig. 9b). The property of liquid silicon changes with the ratio of metallic and covalent bonding [22,23,26–29]. Thus, boron diffusion during laser recovery can be explained by two impurity states: one is high diffusivity state with HDL, and the other low diffusivity state with LDL [17–19]. In a supercooling state, liquid-liquid phase transition (LLPT) occurs as shown by molecular dynamics simulations [25,30–32]. The lower the temperature is, the lower the diffusivity state.

Fig. 10 shows the schematic diagram of dopant transfer mechanism in laser recovery. During laser irradiation, the dopant concentration of melted layer is uniform (Fig. 10a). When laser irradiation stops, the temperature of liquid silicon decreases rapidly, which is similar to a supercooling state, and epitaxial growth begins. In the excimer laser annealing of silicon thin films, the temperature for the supercooling state is 200 K lower than the melting point [33]. According to first-principle molecular dynamics simulation, in the case of pure silicon, the self-diffusive coefficient of silicon in the supercooling state is lower than that in the stable liquid whose temperature is above the melting point of silicon [26]. In other words, convection in the supercooling state is dramatically restrained in comparison with the stable liquid. Therefore, the convection at the solid/liquid interface has insignificant influence on dopant diffusion. During epitaxial growth, however, the boron atoms move towards the solid/liquid interface since the low-diffusivity state favors low temperature as in the supercooling state (Fig. 10b) [17–19]. The boron atoms in the melted layer continuously

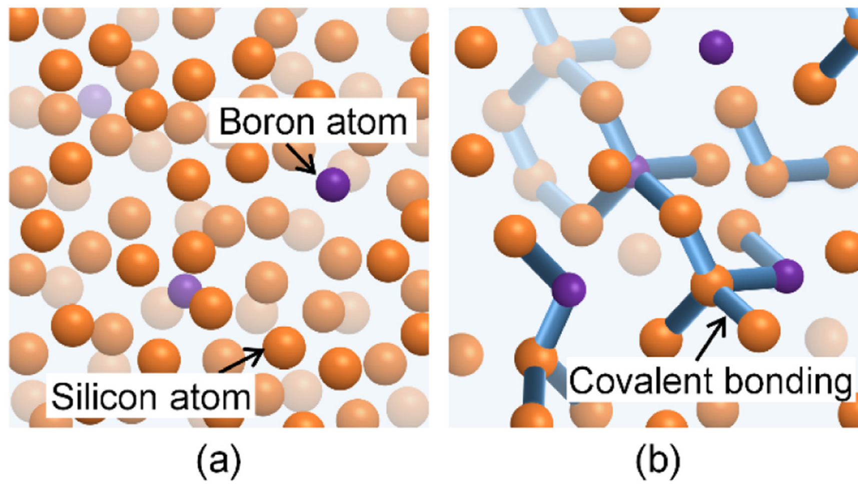

Fig. 9. Schematic diagram of two types of liquid silicon structures with boron atoms: (a) high-density liquid silicon is composed of metallic bonding, and (b) low-density liquid silicon is composed of covalent bonding.

transfer to the solid/liquid interface. As a result, the boron concentration decreases inside the melted layer (Fig. 10c). The segregation coefficient is defined as $k_p = C_s/C_l$, where C_s is dopant concentrations in the solid phase silicon, and C_l is that in the liquid phase silicon. Normally, the segregation coefficient k_p in equilibrium condition for boron in silicon is 0.8 [34,35]. In this case, however, the solid phase silicon cannot sufficiently discharge impurities due to rapid solidification. Consequently, the segregation coefficient becomes $k_p = 1.25$ [16]. Thus, boron concentration becomes the highest at the interface of recrystallized layer and the bulk, resulting in boron pile-up (Fig. 10d).

5. Conclusions

A nanosecond pulsed Nd:YAG laser was used to recover grinding-induced subsurface damage in boron-doped silicon wafers. The laser melted and recrystallized depth was measured by small-angle beveled polishing and subsequent KOH etching. The main conclusions are as follows:

(1) Through small-angle beveled polishing and subsequent KOH etching, a 20 nm-high boundary was generated at the interface of the recrystallized region and the bulk. From this boundary, the laser-induced recrystallized region was successfully visualized and measured.
(2) The recrystallized depth profile follows the Gaussian distribution of the laser beam. A pulse width of 48.4 ns, a fluence of 1.94 J/cm^2 and a peak power of 2.27 kW lead to a recrystallized depth of 909 nm without grooves and pile-ups.
(3) Raman mapping of FWHM and rf-GD-OES analysis showed that crystallinity and boron concentration distribution in the recrystallized region were changed after laser recovery. The dopant concentration was higher at the boundary of the recrystallized region and the bulk, while that in the top surface was lower.
(4) A boron pile-up was detected at the maximum melt depth (642 nm),

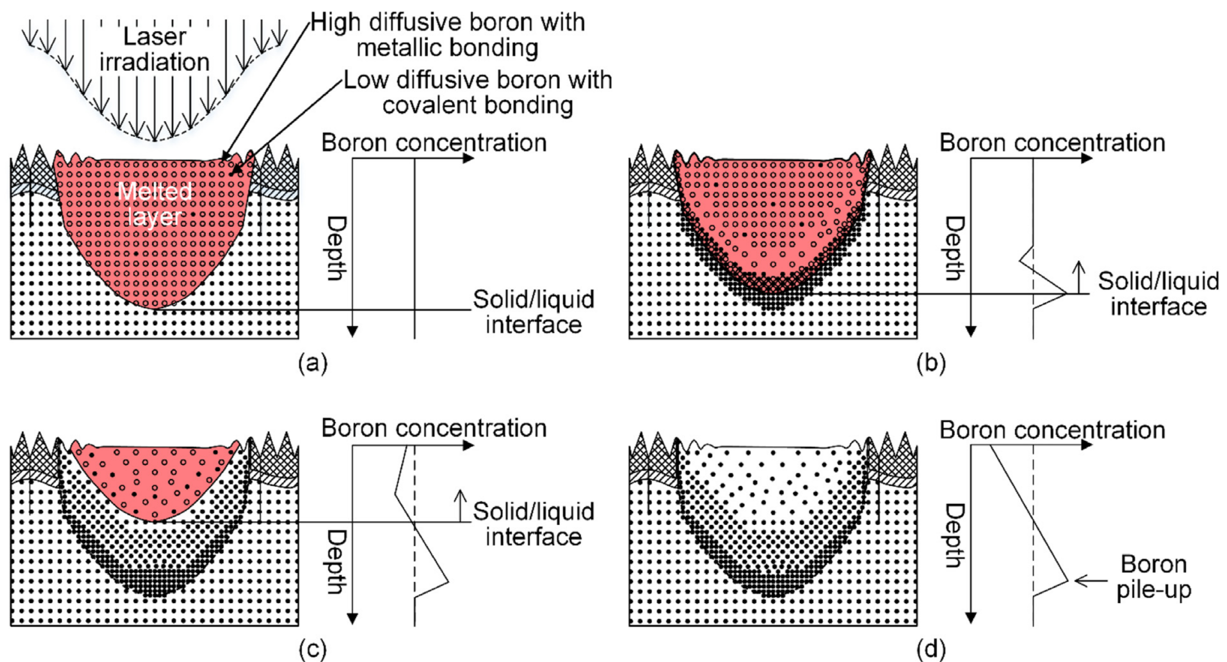

Fig. 10. Schematic diagrams of dopant transfer during recrystallization and resulting dopant concentration profiles: (a) uniform dopant concentration in melted layer during laser irradiation, (b) boron atom transfer to solid/liquid interface, (c) decreasing boron concentration inside the melted layer, (d) the highest boron concentration at the interface of recrystallized layer and the bulk.

in agreement with the directly measured recrystallized depth (653 nm) under a laser peak power of 1.86 kW and a pulse width of 48.4 ns. The boron concentration is controllable by selecting suitable laser parameters.

The findings from this study will greatly contribute to the visualization and clarification of the laser recovery mechanism and the optimization of laser recovery conditions. The methods proposed in this research are applicable to other laser melting/recrystallizing processes for single-crystal silicon, and other single-crystal materials.

References

[1] J. Yan, T. Asami, H. Harada, T. Kuriyagawa, Fundamental investigation of subsurface damage in single crystalline silicon caused by diamond machining, Precis. Eng. 33 (2009) 378–386.
[2] A.M. Kovalchenko, Y.V. Milman, On the cracks self-healing mechanism at ductile mode cutting of silicon, Tribol. Int. 80 (2014) 166–171.
[3] H.N. Li, T.B. Yu, L. Da Zhu, W.S. Wang, Analytical modeling of grinding-induced subsurface damage in monocrystalline silicon, Mater. Des. 130 (2017) 250–262.
[4] Z.J. Pei, G.R. Fisher, J. Liu, Grinding of silicon wafers: a review from historical perspectives, Int. J. Mach. Tools Manuf. 48 (2008) 1297–1307.
[5] H. Ohmori, T. Nakagawa, Analysis of mirror surface generation of hard and brittle materials by ELID (electronic in-process dressing) grinding with superfine grain metallic bond wheels, CIRP Ann. - Manuf. Technol. 44 (1995) 287–290.
[6] J. Yan, F. Kobayashi, Laser recovery of machining damage under curved silicon surface, CIRP Ann. - Manuf. Technol. 62 (2013) 199–202.
[7] J. Yan, T. Asami, T. Kuriyagawa, Response of machining-damaged single-crystalline silicon wafers to nanosecond pulsed laser irradiation, Semicond. Sci. Technol. 22 (2007) 392–395.
[8] J. Yan, S. Sakai, H. Isogai, K. Izunome, Recovery of microstructure and surface topography of grinding-damaged silicon wafers by nanosecond-pulsed laser irradiation, Semicond. Sci. Technol. 24 (2009) 105018.
[9] M.O. Thompson, G.J. Galvin, J.W. Mayer, Melting temperature and explosive crystallization of amorphous silicon during pulsed laser irradiation, Phys. Rev. Lett. 52 (1984) 2360–2364.
[10] H. Azuma, A. Takeuchi, T. Ito, H. Fukushima, T. Motohiro, M. Yamaguchi, Pulsed KrF excimer laser annealing of silicon solar cell, Sol. Energy Mater. Sol. Cells 74 (2002) 289–294.
[11] O. Nast, A.J. Hartmann, Influence of interface and Al structure on layer exchange during aluminum-induced crystallization of amorphous silicon, J. Appl. Phys. 88 (2000) 716–724.
[12] L. Huang, J. Jin, W. Shi, Z. Yuan, W. Yang, Z. Cao, L. Wang, J. Zhou, Q. Lou, Characterization and simulation analysis of laser-induced crystallization of amorphous silicon thin films, Mater. Sci. Semicond. Process. 16 (2013) 1982–1987.
[13] Z. Li, H. Zhang, Z. Shen, X. Ni, Time-resolved temperature measurement and numerical simulation of millisecond laser irradiated silicon, J. Appl. Phys. 114 (2013) 33104.
[14] Z. Yuan, Q. Lou, J. Zhou, J. Dong, Y. Wei, Z. Wang, H. Zhao, G. Wu, Numerical and experimental analysis on green laser crystallization of amorphous silicon thin films, Opt. Laser Technol. 41 (2009) 380–383.
[15] K.K. Ong, K.L. Pey, P.S. Lee, A.T.S. Wee, X.C. Wang, Y.F. Chong, Dopant distribution in the recrystallization transient at the maximum melt depth induced by laser annealing, Appl. Phys. Lett. 89 (2006) 172111.
[16] P.C. Lill, M. Dahlinger, J.R. Köhler, Boron partitioning coefficient above unity in laser crystallized silicon, Materials 10 (2017) 189.
[17] G. Fisicaro, K. Huet, R. Negru, M. Hackenberg, P. Pichler, N. Taleb, A. La Magna, Anomalous impurity segregation and local bonding fluctuation in l-Si, Phys. Rev. Lett. 110 (2013) 117801.
[18] S.F. Lombardo, S. Boninelli, F. Cristiano, G. Fisicaro, G. Fortunato, M.G. Grimaldi, G. Impellizzeri, M. Italia, A. Marino, R. Milazzo, E. Napolitani, V. Privitera, A. La Magna, Laser annealing in Si and Ge: anomalous physical aspects and modeling approaches, Mater. Sci. Semicond. Process. 62 (2017) 80–91.
[19] G. Fisicaro, A. La Magna, Modeling of laser annealing, J. Comput. Electron. 13 (2014) 70–94.
[20] H. Seidel, L. Csepregi, A. Heuberger, H. Baumgartel, Anisotropic etching of crystalline silicon in alkaline solutions, J. Electrochem. Soc. 137 (1990) 3612–3626.
[21] Y.G. Gogotsi, C. Baek, F. Kirscht, Raman microspectroscopy study of processing-induced phase transformations and residual stress in silicon, Semicond. Sci. Technol. 14 (1999) 936–944.
[22] I. Stich, R. Car, M. Parrinello, Bonding and disorder in liquid silicon, Phys. Rev. Lett. 63 (1989) 2240–2243.
[23] J. Sun, R.C. Remsing, Y. Zhang, Z. Sun, A. Ruzsinszky, H. Peng, Z. Yang, A. Paul, U. Waghmare, X. Wu, M.L. Klein, J.P. Perdew, Accurate first-principles structures and energies of diversely bonded systems from an efficient density functional, Nat. Chem. 8 (2016) 831–836.
[24] R.C. Remsing, M.L. Klein, J. Sun, Dependence of the structure and dynamics of liquid silicon on the choice of density functional approximation, Phys. Rev. B 96 (2017) 24203.
[25] J.T. Okada, P.H.L. Sit, Y. Watanabe, Y.J. Wang, B. Barbiellini, T. Ishikawa, M. Itou, Y. Sakurai, A. Bansil, R. Ishikawa, M. Hamaishi, T. Masaki, P.F. Paradis, K. Kimura, T. Ishikawa, S. Nanao, Persistence of covalent bonding in liquid silicon probed by inelastic x-ray scattering, Phys. Rev. Lett. 108 (2012) 67402.
[26] N. Jakse, A. Pasturel, Dynamics of liquid and undercooled silicon: an ab initio molecular dynamics study, Phys. Rev. B - Condens. Matter 79 (2009) 114206.
[27] T. Morishita, How does tetrahedral structure grow in liquid silicon upon supercooling? Phys. Rev. Lett. 97 (2006) 165502.
[28] H. Tanaka, Two-order-parameter description of liquids: critical phenomena and phase separation of supercooled liquids, J. Phys.–Condens. Matter 11 (1999) L159–L168.
[29] H. Tanaka, Simple view of waterlike anomalies of atomic liquids with directional bonding, Phys. Rev. B 66 (2002) 64202.
[30] P. Ganesh, M. Widom, Liquid-liquid transition in supercooled silicon determined by first-principles simulation, Phys. Rev. Lett. 102 (2009) 75701.
[31] N. Jakse, A. Pasturel, Liquid-liquid phase transformation in silicon: evidence from first-principles molecular dynamics simulations, Phys. Rev. Lett. 99 (2007) 205702.
[32] S. Sastry, C. Austen Angell, Liquid–liquid phase transition in supercooled silicon, Nat. Mater. 2 (2003) 739–743.
[33] M. Hatano, S. Moon, M. Lee, K. Suzuki, C.P. Grigoropoulos, Excimer laser-induced temperature field in melting and resolidification of silicon thin films, J. Appl. Phys. 87 (2000) 36–43.
[34] H. Kodera, Diffusion Coefficients of Impurities in Silicon Melt, Jpn. J. Appl. Phys. 2 (1963) 212–219.
[35] R.F. Wood, Model for nonequilibrium segregation during pulsed laser annealing, Appl. Phys. Lett. 37 (1980) 302–304.